Solar Energy Materials & Solar Cells 160 (2017) 182–192

Contents lists available at ScienceDirect

Solar Energy Materials & Solar Cells

journal homepage: www.elsevier.com/locate/solmat

Novel organic photovoltaic polymer blends: A rapid, 3-dimensional morphology analysis using backscattered electron imaging in the scanning electron microscope

Robert C. Masters[a,*], Quan Wan[a], Yiwei Zhang[b], Maurizio Dapor[c], Adrian M. Sandu[d], Chengge Jiao[d], Yangbo Zhou[e], Hongzhou Zhang[e], David G. Lidzey[b], Cornelia Rodenburg[a,*]

[a] Department of Materials Science and Engineering, University of Sheffield, Sir Robert Hadfield Building, Mappin Street, Sheffield S1 3JD, United Kingdom
[b] Department of Physics and Astronomy, University of Sheffield, Hicks Building, Hounsfield Road, Sheffield S3 7RH, United Kingdom
[c] European Centre for Theoretical Studies in Nuclear Physics and Related Areas (ECT*-FBK) and Trento Institute for Fundamental Physics and Applications (TIFPA-INFN), via Sommarive 18, Trento I-38123, Italy
[d] FEI Co. Europe NanoPort, Achtseweg Noord 5, Eindhoven 5651 GG, The Netherlands
[e] School of Physics and CRANN, Trinity College Dublin, Dublin 2, Ireland

ARTICLE INFO

Keywords:
Organic photovoltaics
Morphology
Backscattered electrons
Polymers
Scanning electron microscopy

ABSTRACT

Finding the optimal morphology of novel organic photovoltaic (OPV) polymer blends is a major obstacle slowing the development of more efficient OPV devices. With a focus on accelerating the systematic morphology optimisation process, we demonstrate a technique offering rapid high-resolution, 3-dimensional blend morphology analysis in the scanning electron microscope. This backscattered electron imaging technique is used to investigate the morphological features and length-scales defining the promising PffBT4T-2OD:PC70BM blend system and show how its photovoltaic performance is related to the nature of its phase separation. Low-voltage backscattered electron imaging can be used to probe for structure and domain stacking through the thickness of the film, as well as imaging surface morphology with highly competitive spatial resolution. For reference, we compare our results with equivalent images of the widely studied P3HT:PC60BM blend system. Our results also demonstrate that backscattered electron imaging offers significant advantages over conventional cross-sectional imaging techniques, and show that it enables a fast, systematic approach to control 3-dimensional active layer morphology in polymer:fullerene blends.

1. Introduction

Understanding the nature of phase separation in polymer blends is of great importance for obtaining the optimal performance from various blend systems [1]. Polymer blends have found a wide range of applications in the current energy landscape, having been recently used in novel electrolyte layers in batteries [2] or dye-sensitised solar cells [3,4], for example. However they are particularly prevalent in the field of organic photovoltaics (OPV), where control over the phase-separated morphology of the blend is a critical factor determining the photovoltaic power-conversion efficiency (PCE) [5–9]. One OPV material system that represents the current state-of-the-art is *poly[(5,6-difluoro-2,1,3-benzothiadiazol-4,7-diyl)-alt-(3,3‴-di(2-octyldodecyl)-2,2′;5′,2″;5″,2‴-quaterthiophen-5,5‴-diyl)]*:[6,6]-*phenyl C71 butyric acid methyl ester* (PffBT4T-2OD:PC70BM). This material system has been reported to demonstrate a PCE of up to 10.5% [10]. In spite of its potential, this blend remains somewhat unexplored with no detailed model of its 3-dimensional morphology yet reported.

When fabricated into a photovoltaic device, the polymer component PffBT4T-2OD absorbs incident radiation (forming an exciton), and then acts as an electron donor to the fullerene component (e.g. PC70BM). The photogenerated electrons and holes are then extracted via the fullerene and PffBT4T-2OD phases, respectively [6]. In an efficient photovoltaic blend, there is generally intimate mixing between the polymer and fullerene, as the diffusion length of excitons in many conjugated polymers is limited to < 10 nm. Thus the formation of phase-separation on a similar length scale is generally believed to be essential for efficient exciton dissociation [5]. Additionally, it is

Abbreviations: BSE, Backscattered electron; HeIM, Helium ion microscope

* Corresponding authors.
E-mail addresses: rmasters1@sheffield.ac.uk (R.C. Masters), qwan2@sheffield.ac.uk (Q. Wan), yzhang115@sheffield.ac.uk (Y. Zhang), dapor@ectstar.eu (M. Dapor), adrian.sandu@fei.com (A.M. Sandu), chengge.jiao@fei.com (C. Jiao), yzhou@tcd.ie (Y. Zhou), hozhang@tcd.ie (H. Zhang), d.g.lidzey@sheffield.ac.uk (D.G. Lidzey), c.rodenburg@sheffield.ac.uk (C. Rodenburg).

http://dx.doi.org/10.1016/j.solmat.2016.10.029
Received 25 July 2016; Received in revised form 12 October 2016; Accepted 18 October 2016

necessary to extract dissociated charges from the device without problems relating to charge recombination. In an ideal blend morphology, continuous pathways should exist comprising individual electron- or hole-transporting phases to ensure efficient electron and hole extraction [11]. It is often proposed that phase-separated morphologies composed of columnar structures passing through the film thickness are highly suited to OPV application [12,13], as they combine optimal charge extraction characteristics with a large interface area.

Previous work with X-ray scattering has shown that optimised PffBT4T-2OD:PC70BM blend films are typically characterised by a ~300 nm thick film containing highly-crystalline polymer phases having length-scales of 30–40 nm [10,14]. The phase-separated domains were also shown to be highly pure, with little intermixing between the polymer and fullerene phases. Despite this, the detailed nature of the phase-separated blend morphology within this system was not determined. It is clear that building a detailed picture of the nanoscale structure within a PffBT4T-2OD:PC70BM blend will help in the design of new systems that reach even higher efficiencies [15].

Nanoscale phase-separation in polymer blend films can be revealed using high-resolution imaging techniques such as electron microscopy. Phasecontrast in these films is often low however, and thus the generation of unambiguous electron microscope images can be challenging [16]. Various techniques have been devised to overcome such issues, including the use of energy-filtered techniques in the scanning electron microscope (SEM) [17] or transmission electron microscope (TEM) [18,19] which employ energy-selective electron detection to boost the contrast between the blend components. Additionally, helium ion microscopy (HeIM) replaces the incident electron beam with a helium ion beam and can produce higher quality morphology images as a result [20]. Whilst such techniques are able to generate images with impressive lateral resolution, they require specialist equipment that is not widely available or, in the case of TEM-based methods, require complex and time-consuming preparation of electron transparent samples. This lack of easily accessible information has contributed to the morphology optimisation bottleneck that is hindering the advancement of new OPV systems – a situation well addressed in Ref. [15]. We have implemented low-voltage backscattered electron (BSE) imaging of OPV blends to enable rapid, 3-dimensional morphology characterisation in the SEM.

Previously, BSE imaging of polymer systems has been employed by ‘staining’ one polymer phase with a heavy metal compound to improve BSE contrast [21,22]. This technique typically uses high-energy primary beams, which can lead to poor surface sensitivity and a significant risk of sample damage. More recently, advancements in SEM technology and BSE detector performance have allowed the development of low-energy BSE methods, which have proven effective at combining high spatial-resolution with surface-sensitive material information [23]. This has been used to demonstrate material contrast on polymer films [25,26] using low-voltage BSE imaging without the necessity of staining. The rationale behind the technique is that contrast in BSE images mostly results from material variation, with the BSE signal strength defined by material properties such as atomic packing density or nuclear charge [27]. This is in contrast to conventional SEM imaging using secondary electrons (SE), where imaging contrast largely results from sample topography.

When using BSE to image a polymer blend sample, the interaction depth of the primary electron beam in the sample is an important factor to consider. BSE can theoretically be emitted from any depth up to the maximum interaction depth of the primary beam, although as a rough approximation they are most frequently emitted from the first half of this interaction depth [24,26]. The interaction depth of the primary beam is controlled by the landing energy, E_L, of the beam, with a higher E_L beam interacting up to a larger depth in the sample. As such, the emission depth of BSE can be controlled as a function of E_L. To most effectively probe a polymer film with BSE, E_L must be limited to ensure BSE are emitted from only the film and not the substrate beneath. In this work, we have limited E_L to 3 keV and below for this purpose. This is below energies used in previous polymer BSE imaging experiments [21,22].

For an OPV blend, BSE imaging can be used to probe the nature of the blend morphology over different depths through the film by changing E_L. By imaging with a very low energy, E_L=500 eV, BSE emissions are restricted to the top few nm of the sample, allowing the surface morphology to be probed. Likewise, by tuning E_L such that the BSE emission depth is roughly equal to the thickness of the film, we can probe for structures passing through the whole thickness of the film. When imaging morphology in this case, contrast in a BSE image is highly dependent on whether the BSE emission volume can be largely contained within domains of a single blend component (Fig. 1). If a given blend morphology is comprised of phase-separated structures that are highly aligned through the thickness of the film, it is possible to increase E_L whilst largely containing the BSE emission volume within domains of a single blend component. This results in an image that retains high contrast as a function of beam energy (Fig. 1a). However if BSEs are used to study morphologies with small length scales relative to the dimensions of the BSE emission volume, or disordered blend systems that are heterogeneous through the film thickness, at higher E_L the BSE emission volume at any given point will contain significant amounts of both blend components. In this case, BSE images will show very low phase contrast in the higher beam energy condition, as the BSE signal is averaged over both blend components (Fig. 1b). We can thus easily probe for morphologies showing columnar features or domain stacking ideal for OPV, based upon a BSE image at optimised E_L. We note that similar principles are used as the basis for multi-energy confocal microscopy, typically used to image biological samples deemed too fragile for TEM or focused ion-beam milling techniques [28,29]. However, to date these techniques have only been used at relatively low resolutions, or on stained samples.

Imaging a film using BSE at low E_L brings benefits in the form of reduced knock-on damage from the incident primary beam [30], however additional challenges occur as our BSE detector has inherently poor detection efficiency for low-energy electrons [23]. To overcome this issue, a large negative bias (−4 kV) can be applied to the sample stage in order to improve image quality. This has a three-fold effect [23]: (i) the primary electron beam is generated at higher energy and then decelerated to be incident on the sample with the desired ‘landing energy’ E_L, (ii) electrons emitted from the sample are accelerated and incident on the detector (mounted directly above the sample) with a

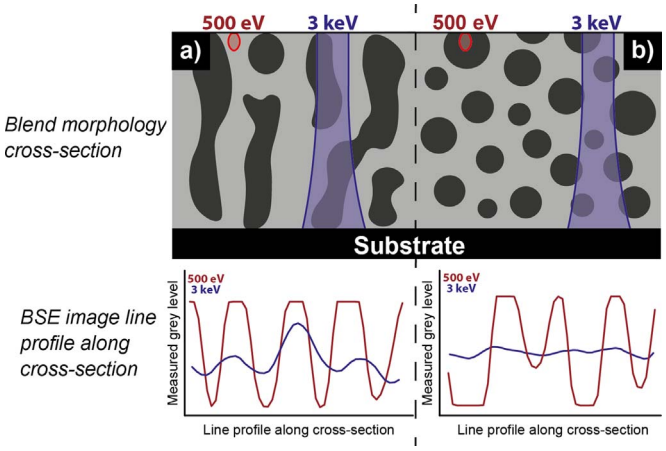

Fig. 1. Schematic of BSE imaging contrast when imaging different morphology types with E_L=500 eV and 3 keV. a) Represents an ordered morphology, with phases highly aligned through the thickness of the film. b) represents a more disordered morphology, with a small, randomly dispersed phase distribution. Red and blue shaded regions represent approximate BSE emission volumes at E_L=500 eV and 3 keV, respectively. (For interpretation of the references to color in this figure legend, the reader is referred to the web version of this article.)

larger energy, increasing the electron detection efficiency, and (iii) electrons emitted over a larger range of angles are 'focused' on to the detector by the applied field. This significantly improves the signal-to-noise ratio in BSE images recorded at low primary beam energies. We note however that care must be taken to understand the effect the stage bias has on emitted electrons, and ensure that our images are formed from BSE in this condition [24]. Details of such considerations can be found in Supporting information for this work.

In this work we explore the surface and sub-surface morphology of a PffBT4T-2OD:PC70BM blend using low-energy BSE imaging. By acquiring the first 3-dimensional image data from this blend, we offer a fresh insight in to the morphological features and length-scales that define the performance of an exciting OPV system. The effectiveness of our imaging technique is verified on reference P3HT:PC60BM samples as well as by comparison with cross-sectional helium-ion microscopy and theoretical considerations from Monte Carlo modelling. Our results suggest that low-energy BSE imaging is an excellent high-throughput technique for 3-dimensional morphological study.

2. Experimental methods

2.1. Sample formation

The PffBT4T-2OD:PC70BM blend films were cast from solution in chlorobenzene and o-dichlorobenzene (1:1 vol ratio) with 3% diiodooctane by volume used as a solvent additive. The polymer and PC70BM solution concentrations were 9 mg mL^{-1} and 10.8 mg mL^{-1} respectively. The solutions were heated on a hot plate at 110 °C and spin-coated on to pre-heated silicon substrates (110 °C) at 1000 rpm in a nitrogen glove box. The substrates were then moved to a hot plate at 100 °C immediately after spin casting for drying.

P3HT:PC60BM samples were formed by spin-coating from chlorobenzene solution. P3HT (purchased from Ossila, brand Merck SP001 with 94.2% regioregularity and M_W=54,200) and PC60BM (purchased from Solenne BV) were separately dissolved in chlorobenzene with concentration 25 mg mL^{-1}, and the solutions left on a hotplate overnight at 70 °C to ensure complete dissolution. Solutions of 1:0.8 (P3HT:PC60BM) ratio by weight were spin-cast on to silicon substrates at 1500 rpm for 40 s. Two P3HT:PC60BM samples were imaged; one in its as-cast state and one that had been thermally annealed at 190 °C for 60 min.

2.2. Imaging of polymer blends

All samples were imaged using a FEI Nova NanoSEM 450 scanning electron microscope equipped with a segmented concentric backscatter (CBS) electron detector acquired from FEI Co. The detector is mounted to the pole piece of the electron column and consists of 4 solid-state components arranged in concentric rings of increasing radius, with a hole in the middle. The CBS detector was optimised for BSE imaging by the enabling only the detector segments (or combination of segments) giving the strongest signal-to-noise ratio. Imaging was performed at 4 mm working distance with immersion lens active, and a −4 kV bias applied to the sample stage.

We note that at the surface of a P3HT:PC60BM blend, a wetting layer of P3HT obscures the film morphology beneath. This layer has been previously shown to impair efforts at imaging surface morphology [17,20], and a similar effect was found for PffBT4T-2OD:PC70BM blend films. When acquiring sub-surface data however the effect of this surface layer on the BSE images is negligible. Therefore, we first imaged pristine films to acquire sub-surface morphology data. Then, to remove the capping layer and obtain clearer surface morphology images, we subjected fresh films to a brief, gentle plasma etch in air (following the procedure of previous works [17,20]). We etched the films for 8 min at low power before immediately placing them in the SEM sample chamber.

Reference images of polymer blend cross-sections were taken with a Zeiss Orion Plus HeIM located at the CRANN facility, Trinity College Dublin. The samples were submersed in liquid nitrogen and cleaved with a diamond knife, then immediately transferred to the microscope chamber. To remove cleaving artefacts the samples were then subject to a plasma clean in air for 24 min. The cross-sections were imaged at a 70° tilt, using a 30 kV primary beam at a working distance of 10 mm.

2.3. Image analysis

In order to perform quantified analysis of the surface morphologies, the images were classified in to binary polymer and fullerene domains using trainable WEKA segmentation in the 'FIJI' distribution of ImageJ [31–33]. This employs machine-learning algorithms that are trained by the user on one or more reference images and then applied to segment other similar images. WEKA segmentation can only be confidently employed in images containing features adhering to well-defined classes. For this reason we only segmented surface-sensitive (E_L=500 eV) images using the WEKA technique in this work. Images taken at higher E_L are complicated by the varying overlap of phases in the BSE imaging signal, making WEKA segmentation difficult. Domain size in higher E_L data was estimated by user-controlled grey level thresholding techniques (as demonstrated in [17]). It should also be noted that WEKA segmentation was used to classify the morphology of P3HT:PC60BM blends, despite the well-documented [17] presence of intermixing between polymer and fullerene phases in this blend type. This was justified as the spatial resolution of our BSE imaging technique is not sufficient to resolve mixed phase material, which tends to form in 2–3 nm wide regions around phase boundaries [17]. Therefore our imaging data shows effectively a 2-phase system at this resolution level.

To measure the important length-scales inherent to the surface morphology, the 'distance maps' [34] of the binary-classified surface morphology images were first calculated using ImageJ. From the distance map image, the morphological features were 'skeletonised' [35], again in ImageJ [36]. The product of the distance map and skeletonised image was taken, such that the distance map was reduced to only display the distance to the nearest phase boundary from the medial axis of any phase. The histogram of this image was taken to demonstrate the distribution of phase radius across the whole image. A more detailed consideration of this process can be found in the Supporting information.

2.4. Monte Carlo modelling of backscattered electron emission

A stepwise Monte Carlo simulation of the interactions of primary electrons with a pure P3HT sample was performed. At each step, the likelihood of the primary electron interacting with the sample via numerous interaction pathways was calculated. In particular, elastic scattering from atomic nuclei, inelastic scattering from atomic electrons, electron-phonon interactions, and electron-polaron interactions were considered and sampled according to common Monte Carlo protocols using random numbers and event probabilities. For each step in the simulation, the nature of the scattering event and the resulting energy loss and scattering angle were calculated. Details of the specific modelling strategy can be found in previous work by Dapor [37]. As inputs to the simulation, the following constants previously determined from P3HT samples were used; electron affinity was taken from Kanai et al. [38], electron energy loss spectra from Engmann et al. [39], band gap data from Nolasco et al. [40], dominant electron trap-depth from Schafferhans et al. [41], and dielectric constants (both static and high-frequency) from Singh et al. [42]. Similar calculations could not be performed for PffBT4T-2OD, as the material properties required as inputs to the simulation are not yet available for this material. It is nonetheless expected that the results of the calculations for P3HT should be largely applicable to PffBT4T-2OD.

The output from this simulation was used to calculate the interaction depth of primary electrons in a P3HT sample for a given primary beam landing energy, in order to estimate the maximum depth of origin in a sample for BSE at different values of E_L. The predicted distribution of emission angles (correcting for the effect of the stage bias) for emitted SE and BSE at all values of E_L used in this work was then calculated. This allows a clear differentiation between signals that originate from BSE and from SE (see Supporting information).

3. Results

3.1. Imaging polymer blend surfaces

Surface morphology images taken from the polymer blend films using E_L=500 V are displayed in Fig. 2. In Fig. 2, parts a, b and c were recorded with identical contrast settings and are presented with no post-processing applied. Features are visible in all images that resemble phase separation in a polymer blend morphology. We have measured the image contrast between pure film samples of PffBT4T-2OD, P3HT, PC70BM and PC60BM, and use this to assign the brighter regions in the images to polymer phases, with the darker regions being assigned to the fullerene (see Supporting Information). The surface morphology of PffBT4T-2OD:PC70BM (see Fig. 2a) has the appearance of highly crystalline PffBT4T-2OD phases with a wide range of lateral diameters (~40–200 nm), separated by narrow regions of different composition (PC70BM).

The PffBT4T-2OD:PC70BM morphology is strikingly different to that observed in a P3HT:PC60BM sample, which shows phase separation on a significantly smaller length scale. In the P3HT blends we observe round, dark fullerene phases interspersing a brighter P3HT matrix, with phases in the thermally annealed sample (see Fig. 2c) appearing coarser and better defined than the as-cast sample (see Fig. 2b). The smallest resolvable features in our surface morphology images (analogous to the lateral imaging resolution) have been measured by the SMART-J plugin for ImageJ [43] as approximately 6 nm.

Fig. 2d, e and f show binary images produced by trainable segmentation in Image J (see Section 2.3), in which the locations of polymer and fullerene phases are defined. Immediately apparent is the area fraction of each blend component at the surface for the three blends. For the P3HT:PC60BM samples, we observe that the measured surface area of PC60BM increases from 22% for the as-cast sample to 43% for the thermally annealed sample. The area fraction of PC70BM at the surface of the PffBT4T-2OD:PC70BM was measured as 25%, which is significantly smaller than the PC70BM weight fraction in this blend (55%). This suggests that the distribution of blend components through the film is not constant – an effect discussed in more detail later in this work.

Fig. 3 shows the distribution of effective domain radius measured from the binary morphology images. The image analysis techniques used to obtain these results can be found in Section 2.3, with a more detailed consideration in the Supporting information. Additionally, the data required to reproduce these plots (and all others in this work) are available at Ref. [44]. These histograms show the distribution of localised domain radius, and can be used to probe the blend morphology length-scales at the surface. Part a) shows the radius distribution for polymer domains, and b) for fullerene domains. For polymer domains, we find that the PffBT4T-2OD:PC70BM film is characterised by a broad size distribution, which peaks in the 10–20 nm range but indicates some phases having a radius that reaches 50 nm. These larger phases are somewhat unexpected given the literature values of ~20–40 nm domain size [10], however we believe they are a result of the increased polymer composition at the surface. For the as-cast and thermally annealed P3HT:PC60BM films however, we determine comparatively narrower size distributions, that indicate P3HT phases have a peak radius in the 5–10 nm range. Considering the fullerene domain size distributions (see Fig. 3b), we find a similarity between the histograms for PffBT4T-2OD:PC70BM and annealed P3HT:PC60BM.

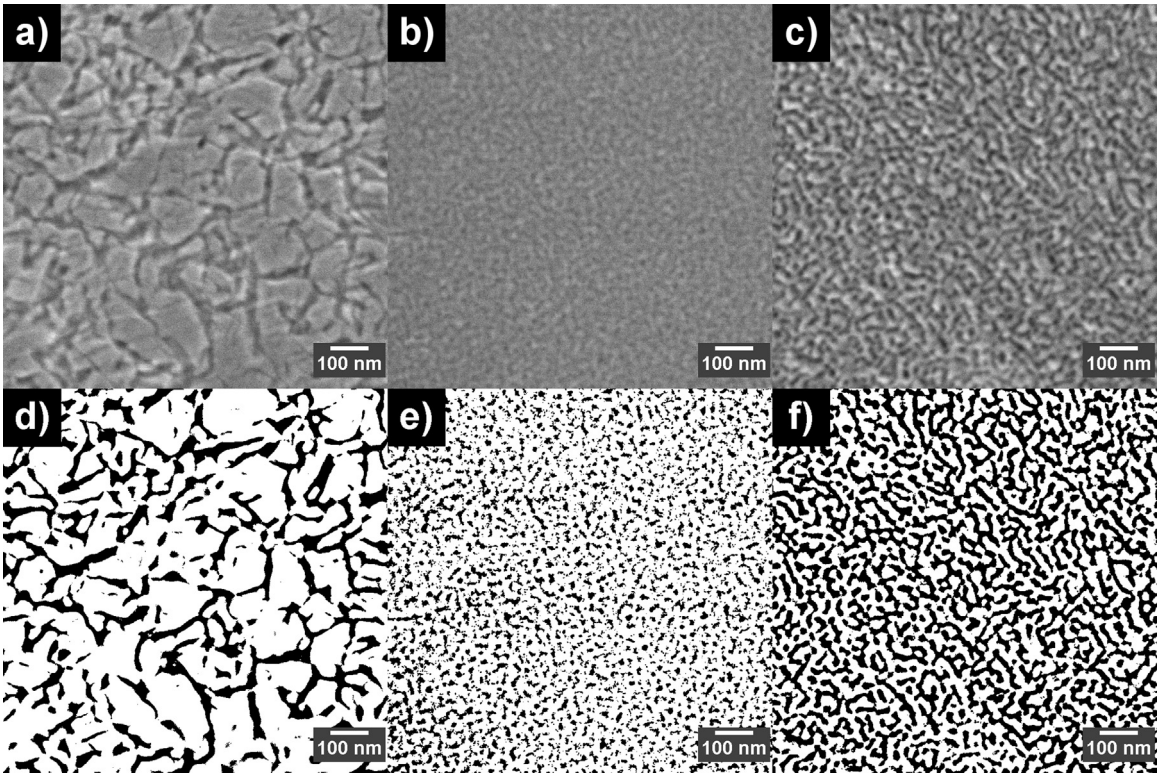

Fig. 2. Surface morphology images of OPV polymer blends imaged using BSE technique at E_L=500 eV. Part a) shows a PffBT4T-2OD:PC70BM film, b) as-cast P3HT:PC60BM, and c) P3HT:PC60BM annealed for 60 min at 190 °C. All samples were subject to an 8-min plasma clean in air prior to imaging. Parts d), e) and f) show parts a), b), and c), respectively, after having been classified in to polymer and fullerene domains by WEKA segmentation. Black regions represent fullerene, white represents polymer.

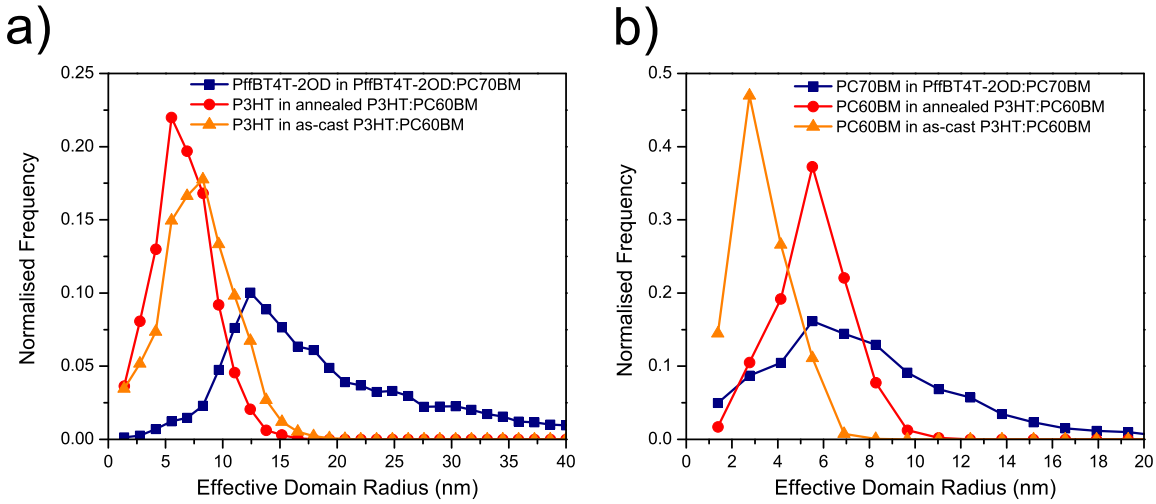

Fig. 3. Domain size histograms for a) polymer phases and b) fullerene phases. The morphological differences between PffBT4T-2OD:PC70BM and different P3HT:PC60BM blend samples can be observed.

Both systems show a domain size distribution that peaks at ~5 nm, although in the PffBT4T-2OD:PC70BM blend the fullerene phases can reach a radius of up to ~20 nm. The as-cast P3HT:PC60BM film however appears to have a significantly smaller average PC60BM domain size, with its domain size distribution peaking at ~3 nm and no domains found with radius larger than 8 nm.

3.2. Probing sub-surface morphology with higher primary beam landing energy

Fig. 4 displays electron micrographs of the PffBT4T-2OD:PC70BM samples as imaged at E_L=500 eV, 1 keV, 2 keV, 3 keV, and 4 keV, respectively. All images are taken from different areas of the sample; taking multiple high-quality images of the same sample area was not possible due to damage caused by a single exposure. The samples in Fig. 4 were not plasma cleaned; whilst probing for sub-surface morphology, a few-nm thick wetting layer has a negligible effect on results. We note that as a result the contrast in the E_L=500 eV image (Fig. 4a) is less clear in comparison to images taken at higher landing energies as well as the E_L=500 eV image taken from a plasma-cleaned PffBT4T-2OD:PC70BM sample (see Fig. 2a).

We find that morphological features can be observed at all E_L used in Fig. 4. In Figs. 4b to 4d, we observe bright features with the appearance of crystallite grains that are separated by narrow, darker regions. Typical features are highlighted in Fig. 4d. Although there are fewer bright crystallite features in images recorded at E_L=2–3 keV (Fig. 4c and d), they appear to be roughly similar in size (lateral diameter of 40–200 nm) to those observed in the surface morphology

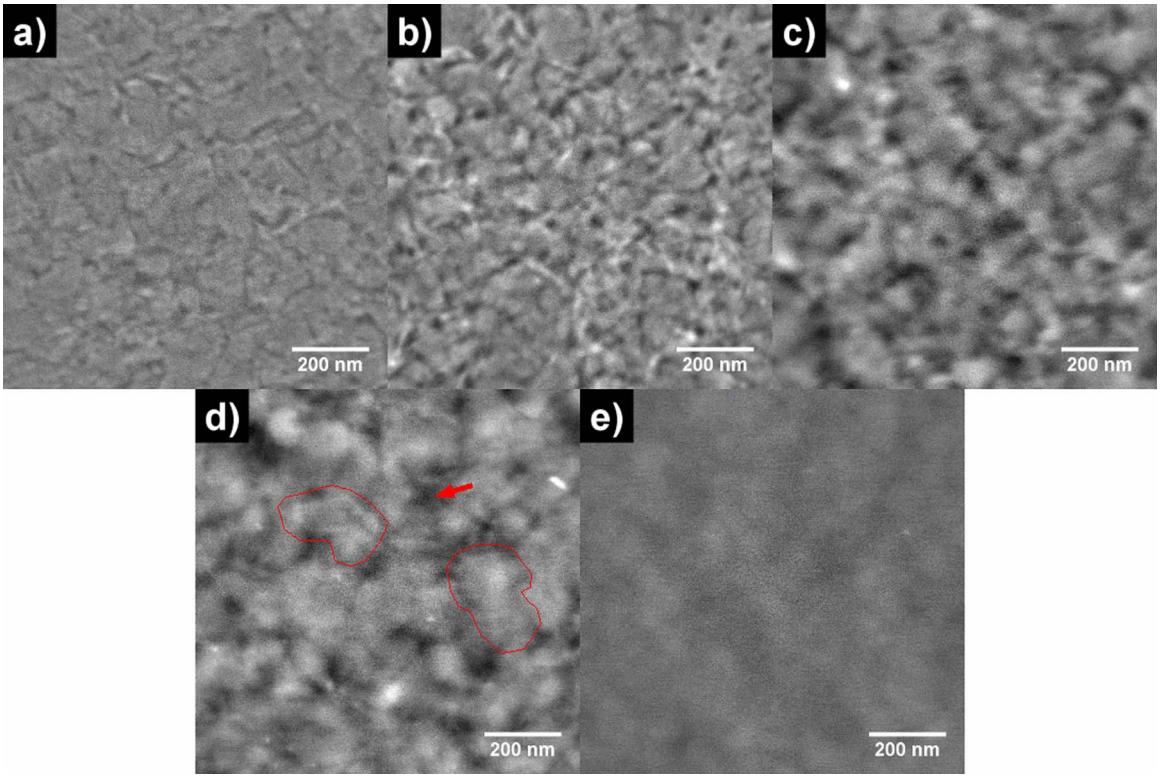

Fig. 4. Images of a PffBT4T-2OD:PC70BM blend imaged with increasing E_L. The film was imaged using E_L= a) 500 eV, (b) 1 keV, (c) 2 keV, (d) 3 keV, and (e) 4 keV. In part d), the arrow highlights a typical highly-aligned PC70BM area, and circled regions highlight typical highly-aligned PffBT4T-2OD areas.

image in Fig. 2a. Notably, the size distribution of such features is narrower in Figs. 4c and 4d, suggesting a greater uniformity in the structure of the phase-separation through the thickness of the film in comparison to the surface.

At E_L=2–3 keV (Fig. 4c–d), a greater fraction of the image has a more 'intermediate' grey level, although the images retain morphology features with high contrast up to E_L=3 keV (Fig. 4d). In the E_L=4 keV image (Fig. 4e), features with a similar appearance to those in Fig. 4d are observed, albeit with reduced contrast and clarity. This may result from some fraction of the image signal originating from the uniform silicon substrate beneath the film. We note that the sharpness and definition of the observed features generally reduces with increasing E_L, indicating a progressive reduction in lateral resolution. We also observed that as E_L was increased, the angular distribution of electrons incident our BSE detector increased in width. This is important evidence suggesting that our images are predominately formed from BSE emission and not SE [24] (see Supporting Information).

To aid the interpretation of the SEM images, we performed similar imaging experiments on P3HT:PC60BM blends. Images of as-cast, unannealed P3HT:PC60BM blends recorded at E_L=500 eV, 1 keV, 2 keV and 3 keV are displayed in Fig. 5, parts a–d respectively. Parts e to h show images recorded from films that had been thermally annealed at 190 °C for 60 min, imaged using the same range of E_L. It can immediately be seen that the films subject to a thermal anneal are characterised by significantly greater image contrast. Once again, we observe that, at E_L=500 eV, only low contrast is visible in images of either sample due to the presence of a surface wetting layer. At E_L=1 keV, some morphological contrast is visible in both samples, although phase separation is more pronounced in the annealed sample. At higher E_L (2–3 keV) however, the samples appear rather different. Image contrast in the as-cast sample has largely disappeared apart from a few larger length-scale features that have the appearance of large aggregates, whereas the annealed sample displays numerous regions with a high degree of contrast. Using E_L=3 keV (see Fig. 5h) we observe a 'background' of intermediate brightness interspersed with small, round features that are either bright or dark. Based upon pure-film contrast (see Supporting information), we interpret these to represent P3HT (bright) or PC60BM (dark) structures that penetrate through a large fraction of the film's thickness at that point.

To perform size analysis on these highly-aligned features, the same image analysis techniques as applied to the surface morphology could not be used. In the E_L=3 keV images, the large and frequent regions of 'intermediate brightness' present made it difficult to confidently classify the image in to regions of polymer and fullerene material showing strong alignment through the film. Instead, user-controlled thresholding techniques as demonstrated in [17] were combined with more conventional particle-size analysis techniques to define the size of high-contrast features in the higher E_L images.

The well-defined dark features in Fig. 5h (assumed to be highly-aligned fullerene domains) have a similar size (15–25 nm radius) and shape to that observed in the PffBT4T-2OD:PC70BM blend (Fig. 4d) recorded under equivalent conditions. In both cases, the fullerene features occupy ~ 3% of the imaged blend area. Example images from our analysis are shown in the Supporting Information to emphasise this finding.

In Fig. 6, we compare the regions of strong polymer phase alignment as determined from thresholded images recorded at E_L=3 keV. We calculate that in the PffBT4T-2OD system, regions of highly aligned polymer account for ~35% of the image area, compared to ~9% in the P3HT:PC60BM system. In both systems a majority of highly-aligned polymer phase domains have a radius between 10 and 30 nm. However this size distribution is narrower in P3HT:PC60BM where the aligned polymer domains are more concentrated in this size range (~90% have < 30 nm radius) and show a significant fraction having a radius < 10 nm. In contrast, the 3 keV images of the PffBT4T-2OD blend system indicate a large fraction (~45%) of aligned polymer regions having a diameter > 30 nm in diameter, with domains having a diameter greater than 100 nm also observed.

3.3. Reference images of polymer blend cross-sections

To see if morphology mapping using higher E_L provides a correct interpretation of 3-dimensional morphology, data from Figs. 4 and 5 were compared with cross-sectional images of cleaved blend films

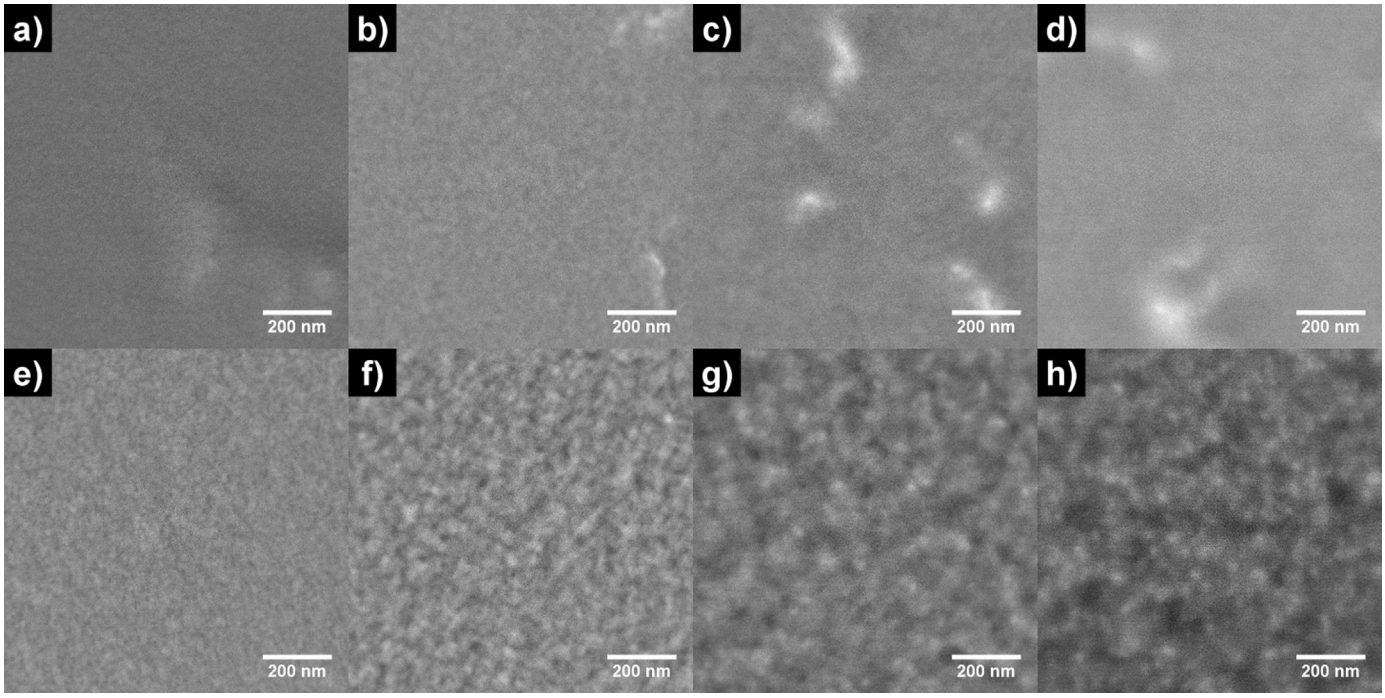

Fig. 5. Images of P3HT:PC60BM blends using with increasing E_L. Parts (a)-(d) show an as-cast blend film imaged using primary beam energies (a) 500 eV, (b) 1 keV, (c) 2 keV and (d) 3 keV. Parts (e)-(h) show a thermally annealed (190 °C for 60 min) blend film imaged at (e) 500 eV, (f) 1 keV, (g) 2 keV and (h) 3 keV. Identical contrast and brightness settings were used for all images.

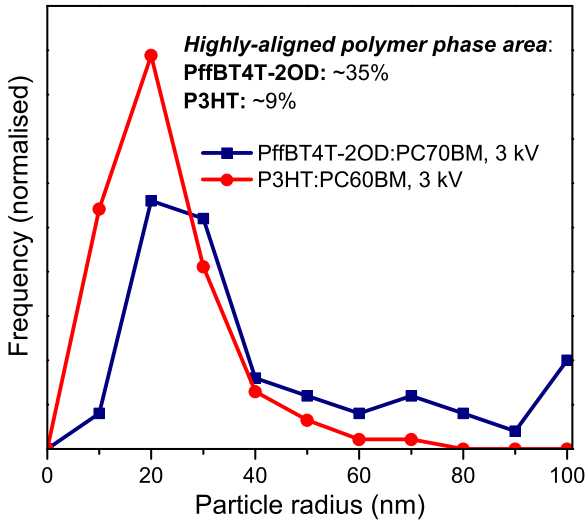

Fig. 6. Sub-surface phase size histogram from E_L=3 keV images of PffBT4T-2OD:PC70BM (Fig. 4d) and annealed P3HT:PC60BM sample (Fig. 5h).

taken with a HeIM, presented in Fig. 7. Specifically, part a) shows a PffBT4T-2OD:PC70BM film, with P3HT:PC60BM films before and after annealing shown in Fig. 7b and c, respectively. It can be seen that the PffBT4T-2OD:PC70BM film is significantly thicker than the P3HT:PC60BM films (~400 nm compared to 130 nm). Cleaving artefacts can be observed in all images, which make the definition of the exact size, shape and distribution of the phase domains difficult. This is especially the case for the PffBT4T-2OD:PC70BM film. A plasma etch was required to remove some artefacts and reveal morphological features in all samples. For the P3HT:PC60BM samples these features appear as voids likely as a result of the preferential etching of one blend component. For the PffBT4T-2OD:PC70BM film in Fig. 7a we observe small features having a highly crystalline appearance, and a variety of narrow, dark features resembling the fullerene domains identified at the surface (Fig. 2a). Some larger dark regions are also observed, however it is difficult to determine whether these are fullerene domains or simply voids in the cross-section. The cross-sectional morphology of the P3HT:PC60BM films is clearer, with small and highly circular domains seen in the as-cast film (Fig. 7b), and a coarser, more column-like morphology seen in the thermally annealed sample (Fig. 7c). Morphological features have been highlighted by arrows in images of the P3HT:PC60BM cross-sections.

3.4. Validation of 3-dimensional morphology data with Monte Carlo simulation

To understand the generation of BSE image data recorded at different E_L, we have simulated the interaction depth of an electron beam in P3HT at different E_L. Fig. 8 shows this depth distribution for E_L=500–3000 eV and can be used to estimate the depth through the film probed by imaging at each E_L value. As previously noted, BSE are typically emitted from around the first half of the primary beam's interaction volume. As such, we can estimate from our simulations that at E_L=500 eV, BSE are emitted from the first ~10 nm of the beam's 20 nm interaction depth. As E_L increases, the interaction depth increases considerably, with the BSE images probing the strength of domain alignment over increasing depths. At E_L=3 keV the BSE signal is generated from the top ~150 nm of the sample, and as such probes for structure over this depth range in a P3HT sample.

By considering the angular distribution of emitted electrons when the SEM stage is subject to biasing, we can confirm the origin of contrast in our images. Our simulations show that as E_L increases, BSE are emitted over a wider distribution of angles. The angle of peak emission (relative to the incidence angle of the beam) also increases at greater E_L. In contrast, the angular distribution of emitted SEs was found to be largely independent of E_L, with SE emissions concentrated at significantly lower angles than BSE, even at E_L=500 eV. This results from a focussing effect of the stage bias field, which has a stronger effect on SE emissions (due to their lower energy) than on BSE. Our simulations suggest that the majority of SEs are in fact not detected in our experimental setup (a detailed consideration can be found in the Supporting information).

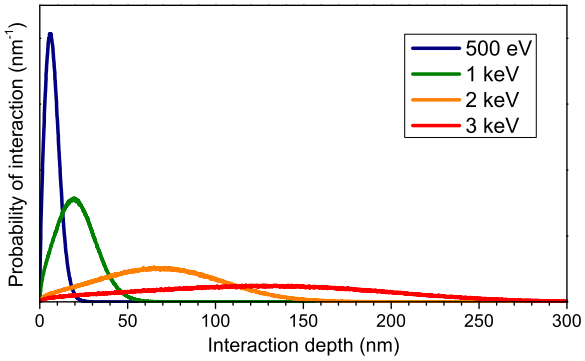

Fig. 8. Depth distribution of primary electron interactions in P3HT as simulated by Monte Carlo model for different values of E_L.

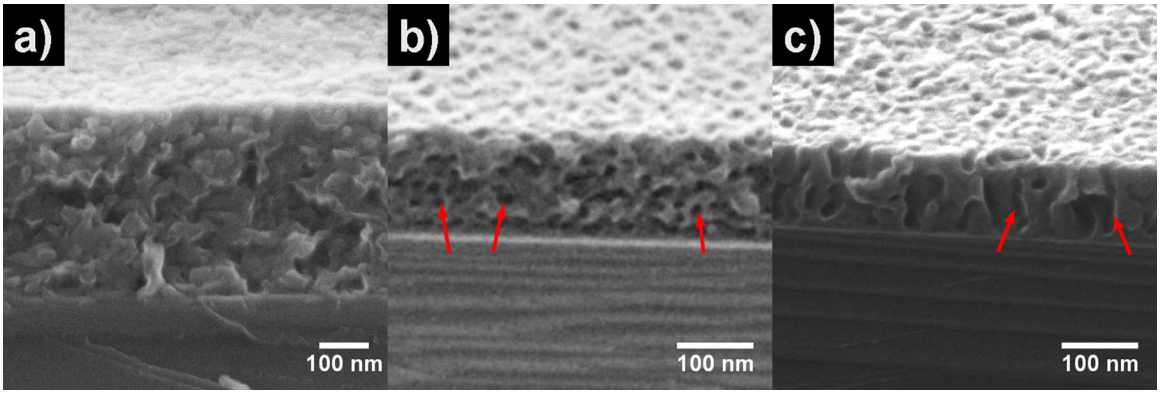

Fig. 7. Cross-sectional images of cleaved polymer blend films, imaged in a helium ion microscope. a) shows a PffBT4T-2OD:PC70BM film, b) an as-cast P3HT:PC60BM blend, and c) P3HT:PC60BM after a 60 min anneal at 190 °C. Arrows show typical phases observed in the P3HT:PC60BM cross-sectional morphology. Note the different size scale bar in part a).

4. Discussion

4.1. Consideration of Monte Carlo modelling, correlation with experimental BSE data

By comparing the results of the Monte Carlo simulations with our experimental data, we can provide a better understanding of our BSE images. Our simulations suggest that only BSEs (carrying information relating to material composition) are emitted at the correct angle and energy necessary to be incident on our BSE detector when the sample stage is biased at 4000 V. We note that our simulations found both the angle of peak emission and spread of the angular distribution for BSE emission to increase with greater E_L. Importantly, this correlates with our imaging experiments (see Supporting information). We are confident therefore that the major constituents of our imaging signal are BSEs, and that material variation is the dominant origin of contrast in the SEM images presented in Figs. 2, 4 and 5.

Fig. 8 shows the change in the implantation depth of incident primary electrons as E_L increases. We have observed that the BSE signal is averaged over a greater fraction of the film's depth as E_L increases. At E_L=3 keV the beam penetrates up to ~300 nm into a P3HT film, with BSE emissions coming from the top ~150 nm of the sample as a result. This indicates that at E_L=3 keV, we are in fact probing for domain structure passing through the whole of a P3HT:PC60BM film. By reducing E_L the BSE signal is emitted from a smaller fraction of the film volume, and probes for structure closer to the film surface (we estimate that BSE emissions occur from the top 10, 25 and 75 nm of the film for a beam energy of E_L=500 eV, 1 keV and 2 keV, respectively). Considering PffBT4T-2OD:PC70BM, we expect that electron beam interactions with this system to be largely similar to those with P3HT:PC60BM. As such the results of our Monte Carlo simulation for P3HT should be broadly applicable. However, the implantation depth of the beam appears larger in the PffBT4T-2OD system. We propose that the drop in image contrast between Fig. 4d (E_L=3 keV) and 4e (E_L=4 keV) corresponds with the point at which the BSE signal begins to originate from the silicon substrate beneath the film. Given the thickness of the film is ~400 nm (Fig. 7a), this implies that, at E_L=3 keV, the BSE emission depth is approaching this thickness. We feel this is a feasible result, however; one would expect a slightly increased electron mean free path in the highly ordered and crystalline PffBT4T-2OD:PC70BM blend. Nonetheless, at E_L=500 eV, the BSE emission depth is smaller than the size of a typical phase in either a P3HT:PC60BM or PffBT4T-2OD:PC70BM system. Imaging at E_L=500 eV, BSE emissions will be isolated in a single material phase at the surface with minimal contribution from the morphology beneath, allowing accurate mapping of surface morphology.

4.2. Experimental validation of BSE technique – 1) surface morphology

The blend surface images presented in Fig. 2 demonstrate the ability of our BSE technique to map surface morphological changes resulting from different film processing conditions. From our images of P3HT:PC60BM films (Fig. 2b-c), we note fullerene phases that are ~3 nm in radius and become larger and better defined in the thermally annealed film. We interpret the improved image contrast seen in the annealed sample as resulting from an increased level of phase purity. This observation is consistent with previous work on P3HT:PC60BM blends in which thermal annealing is seen to improve phase purity and increase the size of PC60BM domains [44–46].

The WEKA segmented images indicate a significantly smaller area fraction of PC60BM (22%) in the surface morphology of the as-cast sample in comparison to the thermally annealed sample. Previous works using neutron reflectivity measurements [48] have identified the presence of a ~20 nm thick PC60BM-depleted layer (separate to the 1–2 nm wetting layer previously discussed [20]) at the top of a comparable as-cast P3HT:PC60BM sample. It was also demonstrated that subjecting a sample to a thermal anneal acts to homogenise the PC60BM concentration throughout the sample, eliminating this PC60BM depleted layer. We observe such effects in our images of the thermally-annealed P3HT:PC60BM sample, where the PC60BM content (as defined by WEKA segmentation) increases to 43%. We note that PC60BM has a relative concentration of 44% (by weight) in our films; as such our results also suggest that PC60BM becomes distributed evenly throughout the film after thermal annealing. In addition to this, the domain size histograms in Fig. 3 show PC60BM domain sizes that peak at ~6 nm in radius for the annealed sample. This result is in agreement with previous studies [20]. We thus conclude that the results from our BSE imaging technique are consistent with other methods used to study polymer:fullerene blends at the surface.

4.3. Experimental validation of BSE technique – 2) through-thickness morphology

When we increased the E_L used for imaging, we observed significant differences between BSE images recorded from as-cast and thermally annealed P3HT:PC60BM blend samples (see Fig. 5). These appear to correspond with differences in the cross-sectional morphology of the blends as imaged by HeIM (Fig. 7b-c). We note that as-cast samples were characterised by low image contrast (see Fig. 5a-d), with phase-separation largely invisible for $E_L > 2$ keV. This finding is consistent with cross-section HeIM imaging shown in Fig. 7b where small, circular domains with little depth penetration were observed. We believe that the BSE emission volume at higher E_L will contain multiple phases of both blend components in this case, resulting in a loss of contrast as the BSE signal is averaged over all phases in this volume. It is also clear that low phase-contrast will also result from the low phase purity present in as-cast P3HT:PC60BM blends [46]. We note the larger bright features present in Fig. 5c-d, which we suspect are larger P3HT aggregates formed in solution.

In the BSE images of thermally annealed samples (Fig. 5e-h), morphological features are clearly observed at all E_L. This is a result of the large surface depth of phases in the more 'columnlike' [49] morphology formed by a thermal anneal. Again, we refer to the HeIM reference image of the annealed sample cross-section in Fig. 7c, where we observe phases that penetrate through a large fraction of the film. For material domains with a large degree of depth penetration, the BSE emission volume up to E_L=3 keV can be mostly contained within that domain, with a high-contrast region observed in BSE images as a result. We therefore interpret the small, high-contrast features seen at E_L=2–3 keV (see Fig. 5g-h) to be P3HT and PC60BM structures highly aligned through the thickness of the film. Our BSE imaging method thus replicates morphology information from cross-sectional HeIM imaging from P3HT:PC60BM blends, without the need for sample cross-sectioning. This demonstrates the effectiveness of low-energy BSE imaging for probing the sub-surface morphology of polymer blends.

4.4. Analysis of PffBT4T-2OD:PC70BM morphology – 1) surface morphology

From the surface image presented in Fig. 2a we conclude that the PffBT4T-2OD:PC70BM surface morphology is highly crystalline in nature, with large crystallites separated by narrow regions of another phase. We believe the bright crystallites to be the polymer phase; a conclusion supported by both the contrast between PffBT4T-2OD and PC70BM in pure-film images (see Supporting information) as well as previous findings that reported that the morphology of a PffBT4T-2OD:fullerene blend is dominated by the initial crystalline aggregation of the polymer phase [10]. The surface data in Fig. 2a closely resembles surface maps of similar blends from atomic force microscopy published

previously [10].

The surface morphology of PffBT4T-2OD:PC70BM is in stark contrast to the morphology of a P3HT:PC60BM blend. The difference in length-scale and ordering between the different blends is exemplified by the segmented binary images and their related domain size histograms. These histograms, derived from our BSE images and calculated from the shortest path to a domain boundary in a given phase (see Supporting information), are a useful morphology analysis tool in the context of OPV blends. They reflect an important aspect of OPV active layer morphology – i.e., the minimum distance an exciton has to diffuse in order to be dissociated in to free charges at a phase boundary.

In the domain size histograms, we observe some notable differences and similarities between the blends. From the polymer histograms shown in Fig. 3a, we note that the PffBT4T-2OD blend has a large peak polymer domain size for an OPV system (~13 nm radius), with the majority of the radius measurements lying in the range 10–20 nm. This matches literature values from both resonant soft x-ray scattering and small-angle neutron scattering experiments well [10,14,50]. The large polymer domain size in the PffBT4T-2OD blend system suggests that the exciton diffusion lengths in PffBT4T-2OD must be larger than in P3HT in order to retain good photovoltaic performance. We suspect that such enhanced diffusion lengths are possible due to the high level of crystallinity in the PffBT4T-2OD phases, as high ordering has been previously shown to improve exciton diffusion in a photovoltaic blend system [51].

The histogram also demonstrates some larger domain sizes, with some polymer phases showing a radius of 40 nm and above, significantly larger than would be expected from this system based upon literature [10]. The presence of these larger phases is likely linked to the large fraction of PffBT4T-2OD material at the surface, where we measure 75% of the surface area to be PffBT4T-2OD despite the blend consisting of only 45% PffBT4T-2OD by weight. This indicates some variation of the relative polymer and fullerene concentrations through the thickness of the film, with the surface morphology showing different relative concentrations with respect to the bulk.

The fullerene domain size histograms (Fig. 3b) indicate similar peak domain radius (~6 nm) for both the annealed P3HT:PC60BM sample and the PffBT4T-2OD:PC70BM sample. This suggests that the fullerene phase is self-ordered in to domains having similar dimensions in two different polymer systems optimised for photovoltaic performance – an intriguing correlation, although the PffBT4T-2OD:PC70BM blend shows a much broader fullerene domain size distribution.

4.5. Analysis of PffBT4T-2OD:PC70BM morphology – 2) through-thickness morphology

The HeIM images of cleaved PffBT4T-2OD blend films (Fig. 7a) are not particularly revealing, as the features and voids present may simply be artefacts remaining from the cleaving process. It should be noted that scanning TEM (STEM) analysis of a focused ion beam-prepared PffBT4T-2OD:PC70BM sample can be used to image the cross-sectional morphology without such cleaving artefacts (see Supporting information for an example). Preparation and imaging of a single cross-section in this way takes several hours to perform however, with sample damage from the invasive preparation and imaging processes a certainty. We can gain insight into the film structure from our non-destructive BSE imaging method in minutes.

It can be seen that the morphology of a PffBT4T-2OD:PC70BM film as recorded using E_L=500 eV (Fig. 4a) appears less clear than that of an otherwise identical sample that had been plasma cleaned (compare Fig. 4a before plasma cleaning with Fig. 2a after plasma cleaning). This perhaps indicates the presence of a similar surface wetting layer to that previously observed in P3HT:PC60BM blends [17]. The surface morphology is seen more clearly in Fig. 4b (E_L=1 keV), which shows similar features to Fig. 4a (E_L=500 eV) but with greater clarity.

It is apparent however that the appearance of the film changes as E_L is increased, with Fig. 4c (E_L=2 keV) and Fig. 4d (E_L=3 keV) displaying morphological features with reduced sharpness in comparison to Figs. 4a to 4b. At greater E_L there are more regions of 'intermediate' contrast surrounding and separating the high-contrast domains of polymer and fullerene material highly aligned normal to the substrate. The intermediate contrast regions represent either areas containing a heterogeneous arrangement of phases through the film or simply boundaries between phases, where the larger interaction volume at E_L=3 keV intersects two or more material domains. Nonetheless it is clear that in both Figs. 4c and 4d we observe high contrast, with both bright and dark areas clearly visible. These high-contrast regions are not necessarily representative of columnar phases, which would imply single material domains that form a continuous charge extraction pathway through the film thickness. However, these regions are strongly indicative of a high level of phase alignment or 'domain stacking' of single-material phases through the film. This is consistent with the impressive photovoltaic performance of the blend system. We define the bright and dark domains in the E_L=3 keV images as highly-aligned polymer and fullerene domains respectively, again based upon the pure film contrast displayed in the Supporting Information.

By thresholding the E_L=3 keV images we were able to approximately quantify the size and frequency of the high-contrast features in Fig. 4d. We estimate that such high-contrast regions of polymer material cover ~35% of the imaged area for the PffBT4T-2OD blend (where PffBT4T-2OD constitutes ~45% of the blend by weight). These high-contrast regions show a size distribution (Fig. 6) that peaks at 10–30 nm (in radius), but also includes a large fraction of domains (45%) having a radius > 30 nm. The size of the smallest features identified in Fig. 4d is approaching the apparent resolution limit of our imaging technique at E_L=3 keV. We therefore note that smaller domain-stacked features may also be present in the film.

To further demonstrate the high level of phase alignment through the depth of the PffBT4T-2OD:PC70BM film morphology, we can compare Fig. 4d with the high-E_L BSE image of the annealed P3HT:PC60BM film (Fig. 5h). Clearly, the bright regions indicating highly-aligned P3HT regions are comparatively smaller and less frequent than the equivalent PffBT4T-2OD phases. This observation is emphasised by comparison of the particle radius histograms in Fig. 6. These give the approximate size distribution of highly-aligned polymer domains in both blend systems. We see that the P3HT blend shows very few highly-aligned regions (~9%) that are larger than 30 nm in radius. Therefore we can conclude that the degree of polymer domain alignment through the film thickness is a key differentiator between the PffBT4T-2OD and P3HT blend morphologies. The PffBT4T-2OD:PC70BM system is comprised by a significantly greater proportion of domains having large surface depth in comparison to P3HT:PC60BM, with the size of these aligned regions also being significantly larger on average.

We identify the dark regions in Fig. 4d as domains of fullerene material strongly aligned through the film thickness. As with the surface morphology, there is a similarity in the size and frequency of aligned fullerene regions in both PffBT4T-2OD and the annealed P3HT blend. From our image analysis, demonstrated in the Supporting Information, the highly-aligned fullerene domains appear in both blend systems with similar size (~15–25 nm radius) and spatial frequency. Once again, the size of the smallest features in our E_L=3 keV images may be resolution-limited here. For the PffBT4T-2OD:PC70BM blend however we note that our analysis suggests that highly-aligned fullerene structures represent only ~3% of the imaged morphology area. This is surprisingly small, as the fullerene comprises approximately 55% of the blend by weight. PffBT4T-2OD blends are known to display extremely high phase purity [10], and as such it is unlikely that much of the remaining fullerene material is dispersed in

mixed phase domains. We believe therefore that PC70BM is dispersed in regions that are not well aligned normal to the substrate, in the large portions of the higher E_L images that are of 'intermediate' brightness and cannot be easily identified as either highly-aligned PffBT4T-2OD or PC70BM domains. In Fig. 4d (E_L=3 keV), we estimate that over 60% of the image can be defined as heterogeneous in this regard, indicating that in terms of morphology there remains significant room for improvement even in this highly-evolved system.

5. Conclusion

We have investigated the surface and sub-surface morphology of a state-of-the-art PffBT4T-2OD:PC70BM blend using a novel BSE imaging method. We found direct evidence of a phase structure with a high degree of domain stacking and formation of material structures that penetrate through a large fraction of the film thickness. The defining length-scales of the surface morphology are in agreement with published work, and the size and distribution of domain-stacked polymer and fullerene regions were also measured. Our combined image data reveals a phase-separated morphology that is expected to be highly beneficial for charge extraction. The BSE imaging technique has been shown to be capable of quickly and easily determining the morphological suitability of a polymer blend for photovoltaic application. As verification we have also applied our BSE imaging method to P3HT:PC60BM blends and successfully compared our data with previous studies, as well as reference images taken using established HeIM techniques.

The ability to probe for structure through the film with no cross-sectioning or complex sample preparation reflects a very powerful sample analysis tool, especially in the context of OPV where morphology plays a significant role in defining the performance of a given system [15]. We believe that this BSE imaging technique should be particularly attractive as a tool to aid the development of new, advanced OPV systems, complimenting already established high-speed techniques [52]. By providing scope for high-resolution, 3-dimensional morphology analysis with unprecedented throughput, the technique enables swift analysis and subsequent optimisation of morphology in novel OPV material systems.

Acknowledgements

We thank the Faculty of Engineering at the University of Sheffield and the Grantham Centre for Sustainable Futures for funding RM's PhD studentship. We also thank the UK EPSRC for supporting this research through grants EP/J017361/1 "Supergen Supersolar Hub" and EP/M025020/1 "High resolution mapping of performance and degradation mechanisms in printable photovoltaic devices". MD was supported by a visiting professorship from the Leverhulme Trust (VP1-2014-011), and Instituto Nazionale di Fisica Nucleare (INFN) through the Supercalcolo agreement with FBK. Y. Zhang thanks the University of Sheffield for providing a PhD scholarship. The Royal Society funded a collaboration with Y. Zhou and HZ (IE140211). CR is supported by EPSRC grant EP/N008065/1. We would also like to extend thanks to the Sorby Centre for Electron Microscopy at the University of Sheffield for the technical support provided.

Appendix A. Supporting information

Supplementary data associated with this article can be found in the online version at doi:10.1016/j.solmat.2016.10.029.

References

[1] E. Moons, Conjugated polymer blends: linking film morphology to performance of light emitting diodes and photodiodes, J. Phys. Condens. Matter 14 (2002) 12235–12260.
[2] J.R. Nair, M. Destro, F. Bella, G.B. Appetecchi, C. Gerbaldi, Thermally cured semi-interpenetrating electrolyte networks (s-IPN) for safe and aging-resistant secondary lithium polymer batteries, J. Power Sources 306 (2016) 258–267.
[3] M. Gerosa, A. Sacco, A. Scalia, F. Bella, A. Chiodoni, M. Quaglio, et al., Toward totally flexible dye-sensitized solar cells based on titanium grids and polymeric electrolyte, IEEE J. Photovolt. 6 (2016) 498–505.
[4] R. Shanti, F. Bella, Y.S. Salim, S.Y. Chee, S. Ramesh, K. Ramesh, Poly(methyl methacrylate-co-butyl acrylate-co-acrylic acid): physico-chemical characterization and targeted dye sensitized solar cell application, Mater. Des. 108 (2016) 560–569.
[5] J. Nelson, Polymer: fullerene bulk heterojunction solar cells, Mater. Today 14 (2011) 462–470.
[6] H. Hoppe, N.S. Sariciftci, Organic solar cells: an overview, J. Mater. Res. 19 (2011) 1924–1945.
[7] N.D. Treat, M.L. Chabinyc, Phase separation in bulk heterojunctions of semiconducting polymers and fullerenes for photovoltaics, Annu. Rev. Phys. Chem. 65 (2014) 59–81.
[8] C. Gao, Z. Qiao, K. Shi, S. Chen, Y. Li, G. Yu, et al., Hexa-peri-hexabenzocoronene and diketopyrrolopyrrole based D-A conjugated copolymers for organic field effect transistor and polymer solar cells, Org. Electron. 38 (2016) 245–255.
[9] Y.-C. Huang, H.-C. Cha, C.-Y. Chen, C.-S. Tsao, Morphological control and performance improvement of organic photovoltaic layer of roll-to-roll coated polymer solar cells, Sol. Energy Mater. Sol. Cells 150 (2016) 10–18.
[10] Y. Liu, J. Zhao, Z. Li, C. Mu, W. Ma, H. Hu, et al., Multiple cases of high-efficiency polymer solar cells, Nat. Commun. 5 (2014) 1–8.
[11] A.J. Heeger, 25th Anniversary Article: bulk heterojunction solar cells: understanding the mechanism of operation, Adv. Mater. (2013) 10–28.
[12] Y.C. Tseng, S.B. Darling, Block copolymer nanostructures for technology, Polymers 2 (2010) 470–489.
[13] W. Cai, X. Gong, Y. Cao, Polymer solar cells: recent development and possible routes for improvement in the performance, Sol. Energy Mater. Sol. Cells 94 (2010) 114–127.
[14] W. Ma, G. Yang, K. Jiang, J.H. Carpenter, Y. Wu, X. Meng, et al., Influence of processing parameters and molecular weight on the morphology and properties of high-performance PffBT4T-2OD:PC71BM organic solar cells, Adv. Energy Mater. 5 (2015).
[15] N.E. Jackson, B.M. Savoie, T.J. Marks, L.X. Chen, M.A. Ratner, The next breakthrough for organic photovoltaics?, J. Phys. Chem. Lett. 6 (2015) 77–84.
[16] M. Pfannmöller, W. Kowalsky, R.R. Schröder, Visualizing physical, electronic, and optical properties of organic photovoltaic cells, Energy Environ. Sci. 6 (2013) 2871–2891.
[17] R.C. Masters, A.J. Pearson, T.S. Glen, F.-C. Sasam, L. Li, M. Dapor, et al., Sub-nanometre resolution imaging of polymer–fullerene photovoltaic blends using energy-filtered scanning electron microscopy, Nat. Commun. 6 (2015) 6928.
[18] M. Pfannmöller, H. Flügge, G. Benner, I. Wacker, C. Sommer, M. Hanselmann, et al., Visualizing a homogeneous blend in bulk heterojunction polymer solar cells by analytical electron microscopy, Nano Lett. 11 (2011) 3099–3107.
[19] R. Murray, N. Rujisamphan, S.I. Shah, Predicting current from cross section images of organic photovoltaic devices, Sol. Energy Mater. Sol. Cells 134 (2015) 231–235.
[20] A.J. Pearson, S.A. Boden, D.M. Bagnall, D.G. Lidzey, C. Rodenburg, Imaging the bulk nanoscale morphology of organic solar cell blends using helium ion microscopy, Nano Lett. 11 (2011) 4275–4281.
[21] G. Goizueta, T. Chiba, T. Inoue, Phase morphology of polymer blends: scanning electron microscope observation by backscattering from a microtomed and stained surface, Polymer 33 (1992) 886–888.
[22] G. Bar, E. Tocha, E. Garcia-Meitin, C. Todd, J. Blackson, New routes to high resolution and automated polymer morphology microscopy via scanning electron microscopy, Macromol. Symp. 282 (2009) 128–135.
[23] D. Phifer, L. Tuma, T. Vystavel, P. Wandrol, R.J. Young, Improving SEM imaging performance using beam deceleration, Micros. Today 17 (2009) 40–49.
[24] Q. Wan, R.C. Masters, D. Lidzey, K.J. Abrams, M. Dapor, R.A. Plenderleith, et al., Angle selective backscattered electron contrast in the low-voltage scanning electron microscope: Simulation and experiment for polymers, Ultramicroscopy 171 (2016) 126–138.
[25] R.C. Masters, Q. Wan, Y. Zhou, A.M. Sandu, M. Dapor, H. Zhang, et al., Application of low-voltage backscattered electron imaging to the mapping of organic photovoltaic blend morphologies, J. Phys. Conf. Ser. 644 (2015) 12017.
[26] Q. Wan, R.A. Plenderleith, M. Dapor, S. Rimmer, F. Claeyssens, C. Rodenburg, Separating topographical and chemical analysis of nanostructure of polymer composite in low voltage SEM, J. Phys. Conf. Ser. 644 (2015) 12018.
[27] W. Zhou, R.P. Apkarian, Z.L. Wang, D.C. Joy, Fundamentals of scanning electron microscopy, in: W. Zhou, Z.L. Wang (Eds.), Scanning Microsc. Nanotechnol., Springer New York, New York, NY, 2006, pp. 1–40.
[28] F. Boughorbel, X. Zhuge, P. Potocek, B. Lich, SEM 3D reconstruction of stained bulk samples using landing energy variation and deconvolution, Microsc. Microanal. 18 (2012) 560–561.
[29] V. Marx, Neurobiology: brain mapping in high resolution, Nature 503 (2013) 147–152.
[30] J. Butler, D.C. Joy, G. Bradley, S. Krause, Low-voltage scanning electron microscopy of polymers, Polymer 36 (1995) 1781–1790.
[31] C.A. Schneider, W.S. Rasband, K.W. Eliceiri, NIH Image to ImageJ: 25 years of image analysis, Nat. Methods 9 (2012) 671–675.
[32] J. Schindelin, I. Arganda-Carreras, E. Frise, V. Kaynig, M. Longair, T. Pietzsch, et al., Fiji: an open-source platform for biological-image analysis, Nat. Methods 9 (2012) 676–682.
[33] M. Hall, E. Frank, G. Holmes, B. Pfahringer, P. Reutemann, I.H. Witten, The WEKA data mining software, ACM SIGKDD Explor. Newsl. 11 (2009) 10.

[34] P.E. Danielsson, Euclidean distance mapping, Comput. Graph. Image Process 14 (1980) 227–248.
[35] A.K. Jain, Fundamentals of Digital Image Processing, Prentice Hall, Englewood Cliffs, NJ, 1989.
[36] T.C. Lee, R.L. Kashyap, C.N. Chu, Building skeleton models via 3-D medial surface axis thinning algorithms, CVGIP Graph. Model. Image Process. 56 (1994) 462–478.
[37] M. Dapor, Transport of Energetic Electrons in Solids, Springer, Berlin, 2014.
[38] K. Kanai, T. Miyazaki, H. Suzuki, M. Inaba, Y. Ouchi, K. Seki, Effect of annealing on the electronic structure of poly(3-hexylthiophene) thin film, Phys. Chem. Chem. Phys. 12 (2010) 273–282.
[39] S. Engmann, V. Turkovic, P. Denner, H. Hoppe, G. Gobsch, Optical order of the polymer phase within polymer/fullerene blend films, J. Polym. Sci. Part B Polym. Phys. 50 (2012) 1363–1373.
[40] J.C. Nolasco, R. Cabre, J. Ferré-Borrull, L.F. Marsal, M. Estrada, J. Pallarès, Extraction of poly (3-hexylthiophene) (P3HT) properties from dark current voltage characteristics in a P3HT/n-crystalline-silicon solar cell, J. Appl. Phys. 107 (2010) 44505.
[41] J. Schafferhans, A. Baumann, A. Wagenpfahl, C. Deibel, V. Dyakonov, Oxygen doping of P3HT:PCBM blends: influence on trap states, charge carrier mobility and solar cell performance, Org. Electron. 11 (2010) 1693–1700.
[42] R. Singh, R.K. Singh, J. Kumar, R. Kant, V. Kumar, The origin of DC electrical conduction and dielectric relaxation in pristine and doped poly(3-hexylthiophene) films, J. Polym. Sci. Part B Polym. Phys. 48 (2010) 1047–1053.
[43] D.C. Joy, SMART - a program to measure SEM resolution and imaging performance, J. Microsc. 208 (2002) 24–34.
[44] Dataset for figures in Novel organic photovoltaic polymer blends: A rapid, 3-dimensional morphology analysis using backscattered electron imaging in the scanning electron microscope. ⟨http://https://dx.doi.org/10.15131/shef.data.4004088.v1⟩ (accessed 12.10.16).
[45] A.J. Pearson, T. Wang, R.A.L. Jones, D.G. Lidzey, P. a. Staniec, P.E. Hopkinson, et al., Rationalizing phase transitions with thermal annealing temperatures for P3HT:PCBM organic photovoltaic devices, Macromolecules 45 (2012) 1499–1508.
[46] D.E. Motaung, G.F. Malgas, C.J. Arendse, S.E. Mavundla, C.J. Oliphant, D. Knoesen, The influence of thermal annealing on the morphology and structural properties of a conjugated polymer in blends with an organic acceptor material, J. Mater. Sci. 44 (2009) 3192–3197.
[47] Y.-C. Huang, Y.-C. Liao, S.-S. Li, M.-C. Wu, C.-W. Chen, W.-F. Su, Study of the effect of annealing process on the performance of P3HT/PCBM photovoltaic devices using scanning-probe microscopy, Sol. Energy Mater. Sol. Cells 93 (2009) 888–892.
[48] A.J. Parnell, A.D.F. Dunbar, A.J. Pearson, P. a. Staniec, A.J.C. Dennison, H. Hamamatsu, et al., , Depletion of PCBM at the cathode interface in P3HT/PCBM thin films as quantified via neutron reflectivity measurements, Adv. Mater. 22 (2010) 2444–2447.
[49] J.S. Moon, J.K. Lee, S. Cho, J. Byun, A.J. Heeger, “Columnlike” structure of the cross-sectional morphology of bulk heterojunction materials, Nano Lett. 9 (2009) 230–234.
[50] Y.Zhang, A.J.Parnell, F.Pontecchiani, J.F.K.Cooper, R.L.Thompson, R.A.L.Jones, et al., 1,8-diiodooctane enables domain coarsening upon thermal annealing to increase power conversion efficiency in PffBT4T-2OD/PC71BM devices, Submitted. (n.d.)
[51] M. Sim, J. Shin, C. Shim, M. Kim, S.B. Jo, J.-H. Kim, et al., Dependence of exciton diffusion length on crystalline order in conjugated polymers, J. Phys. Chem. C 118 (2014) 760–766.
[52] F.C. Krebs, M. Jørgensen, 2D Characterization of OPV from single and tandem cells to fully roll-to-roll processed modules with and without electrical contact, Adv. Opt. Mater. 2 (2014) 465–477.